PAPER

Check for updates

Manganese and selenium co-doped CeO_2@Co_3O_4 porous core–shell nanospheres for enhanced oxygen evolution reactions†

Xianggang Huang,‡[a] Xin Wang,‡[b] Mengling Zhang,[a] Qilei Jiang,[a] Zheng Qin,[a] Yingxin Liu,[a] Yan Hou,[a] Xueqin Cao*[a] and Hongwei Gu ✩ *[a]

As one of the semi-reactions of water splitting, electrocatalytic oxygen evolution reactions (OERs) are key process to generate sustainable energy. Co-based spinel oxides are deemed as promising OER electrocatalysts, but the low intrinsic activity limits their further practical applications. Herein, we report an effective strategy to synthesize CoCeMn coordination-driven self-assembled aggregates (CDSAAs) by a one-pot multi-step method. It is different from the common mixed addition method to synthesize trimetallic nanomaterials. Subsequently, CoCeMn-CDSAAs served as self-templates, and Mn and Se co-doped CeO_2@Co_3O_4 porous core–shell nanospheres (MnSe–CeO_2@Co_3O_4) were obtained after calcination and selenization treatments. It is worth mentioning that CeO_2 and the doping Mn/Se elements increase the oxygen vacancy content and the ratio of Co^{3+}/Co^{2+} on the surface respectively and can effectively accelerate the four-electron transfer process of OERs. Moreover, the special porous core–shell structure exposes more active sites and is also useful for boosting OER performance. When explored as an anode electrocatalyst for OERs, MnSe–CeO_2@Co_3O_4 exhibits excellent OER performance (284 mV@10 mA cm^{-2}) and a long-time stability of 40 h in an alkaline medium. This work provides a feasible idea for the construction of multi-component porous core–shell nanoelectrocatalysts with non-noble metals.

1. Introduction

With the rapid increase in energy demand and the intensification of global environmental problems, it is important to develop renewable and clean energy sources.[1,2] Electrolysis of water is a promising way to generate pure hydrogen. However, the slow four-electron transfer process of oxygen evolution reactions (OERs) at the anode has restricted the efficiency of water splitting.[3–5] Although noble metal catalysts such as RuO_2 exhibit excellent OER performance, the high price and low natural abundance hinder their large-scale applications.[6] Therefore, it is urgent to develop efficient and stable non-noble metal electrocatalysts for OERs.

In recent years, spinel transition-metal oxides have received extensive attention from researchers around the world due to

their low price, easy availability and abundant storage.[7,8] Furthermore, Co_3O_4, as a cobalt-based spinel oxide, has been regarded as a potential OER electrocatalyst because of its excellent performance in an alkaline medium.[9,10] However, the practical application of pure Co_3O_4 is limited because of its poor intrinsic conductivity and insufficient active sites.[11] Developing efficient OER electrocatalysts with competitive price, low overpotential and long-time stability is challenging, and researchers have made considerable efforts to boost the OER performance of Co_3O_4 through these years.

On the one hand, the intrinsic activity of the materials can be improved obviously by increasing oxygen vacancies or doping other elements.[12–14] CeO_2, as a rare earth oxide, has been considered as an effective synergist for OERs due to its excellent redox ability and abundant oxygen vacancies.[15,16] After introducing CeO_2, the valence state conversion between Ce^{3+} and Ce^{4+} can accelerate electron transfer and increase the oxygen vacancies of materials, thus promoting the catalytic activity for OERs.[17] Qiu *et al.* constructed a special CeO_2/Co_3O_4 heterojunction interface with enhanced OER performance, which is attributed to the abundant oxygen vacancies and interfacial coupling effect between the components.[18] Moreover, doping other elements such as manganese (Mn),[19] iron (Fe),[20] selenium

[a] Key Laboratory of Organic Synthesis of Jiangsu Province, College of Chemistry, Chemical Engineering and Materials Science and Collaborative Innovation Center of Suzhou Nano Science and Technology, Soochow University, Suzhou 215123, P. R. China. E-mail: hongwei@suda.edu.cn, xqcao@suda.edu.cn

[b] Key Laboratory of Rare Mineral of hubei Province, Ministry of Natural Resources, Hubei Geological Experimental Testing Center, Wuhan 430034, P. R. China

† Electronic supplementary information (ESI) available. See DOI: https://doi.org/10.1039/d2ya00315e

‡ These authors contributed equally.

(Se),[21] and sulfur (S)[22] can regulate the electronic structure of catalysts, resulting in faster four-electron transfer progress and is regarded as a promising method to enhance their intrinsic activity. Moreover, a higher content of Co^{3+} in nanomaterials also contributes to better OER performance.[23,24] Qi *et al.* designed a Mn and S dual-doped Co_3O_4 electrode array for efficient OERs. The excellent OER performance is attributed to their improved electrical conductivity and increasing ratio of Co^{3+}/Co^{2+} after doping with Mn and S elements.[25] On the other hand, appropriate morphology designs such as core–shell structure can expose more active sites and facilitate charge transfer in materials.[26,27] Currently, numerous strategies have been developed to construct core–shell structures such as the Kirkendall effect,[28] Ostwald ripening,[29] and template method.[30] Zhang *et al.* synthesized pure CeO_2 core–shell nanospheres by a simple self-template and calcination method.[31] However, the preparation of multielement core–shell hybrid nanomaterials is still a great challenge and has rarely been reported.

Herein, we report a facile approach to fabricate CoCeMn coordination-driven self-assembled aggregates (CDSAAs) by a simple one-pot multi-step method, in which the Ce element is enriched at the core of the solid nanosphere. Subsequently, CoCeMn-CDSAAs as self-temples were calcined in air to form Mn-doped $CeO_2@Co_3O_4$ porous core–shell nanospheres ($Mn–CeO_2@Co_3O_4$). Finally, $Mn–CeO_2@Co_3O_4$ was selenized in an Ar atmosphere and Se/Mn co-doped $CeO_2@Co_3O_4$ porous core–shell nanospheres ($MnSe–CeO_2@Co_3O_4$) were obtained (Fig. S1, ESI†). CeO_2 can effectively increase the oxygen vacancy content on the surface, which is helpful for promoting the OER performance. After doping of Se and Mn elements, the alteration of Co electronic structure can not only increase the electrical conductivity, but also improve the ratio of Co^{3+}/Co^{2+} of the nanomaterial, which both contribute to enhancing the OER kinetic properties. In an alkaline medium of 1.0 M KOH, $MnSe–CeO_2@Co_3O_4$ exhibits a low overpotential of 284 mV@ 10 mA cm^{-2}, which is much lower than that of Co-oxides (419 mV@10 mA cm^{-2}). In addition, they also exhibit the lowest Tafel slope of 94 mV dec^{11} and excellent stability of 40 h.

2. Results and discussion

As described in Scheme 1, $MnSe–CeO_2@Co_3O_4$ was synthesized *via* a simple one-pot multi-step reaction, calcination and selenization strategy. First, $Ce(OAc)_3$, $Mn(OAc)_2$, and $Co(OAc)_2$ (molar ratio of 1:4:8) were added in turn to a methanolic solution of HL_{10}, and a CoCeMn-CDSAA precursor was successfully synthesized by coordination assembly of metal ions and HL_{10}. Subsequently, $Mn–CeO_2@Co_3O_4$ was obtained after calcination of CoCeMn-CDSAAs in an air atmosphere. On the one hand, the enrichment of Ce elements in the CoCeMn-CDSAAs contributes to the formation of core–shell structures, which can be confirmed by the later characterization. On the other hand, CO_x and H_2O derived from the decomposition of organic ligands facilitate the generation of porous structures in the process of calcination. Finally, $MnSe–CeO_2@Co_3O_4$ was obtained by selenization of
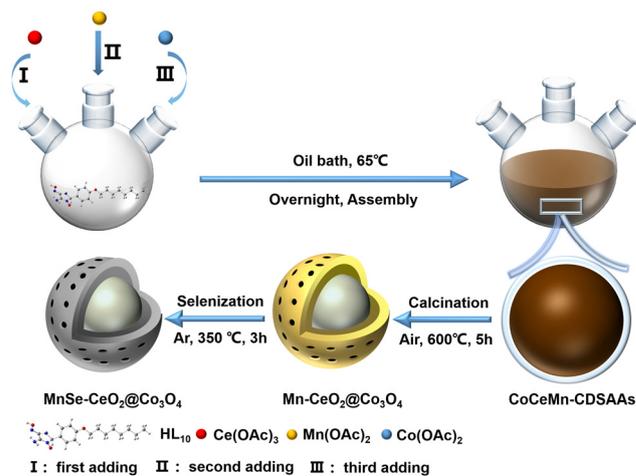
Scheme 1 Schematic illustration of the synthesis procedure of $MnSe–CeO_2@Co_3O_4$.

$Mn–CeO_2@Co_3O_4$ in an Ar atmosphere. The $MnSe–CeO_2@Co_3O_4$ porous core shell nanospheres with high oxygen vacancy contents and a high ratio of Co^{3+}/Co^{2+} ultimately exhibit excellent electrocatalytic performance.

From the perspective of morphology, CoCeMn-CDSAAs are smooth solid nanospheres with a diameter of about 1 μm (Fig. 1(a) and (b)). Moreover, the larger magnification TEM image reveals that there is a darker shadow inside the nanospheres (Fig. 1(c)). A series of CoCeMn-CDSAAs with different metal ratios can be easily obtained when adjusting the amount of different metal salts added in the one-pot multi-step method. Meanwhile, it can be illustrated by inductively coupled plasma-atomic emission spectroscopy (ICP-AES) that the elemental ratios of Co and Ce roughly match the feeding ratios and the Mn element is mainly doped by small amounts (Table S1, ESI†).
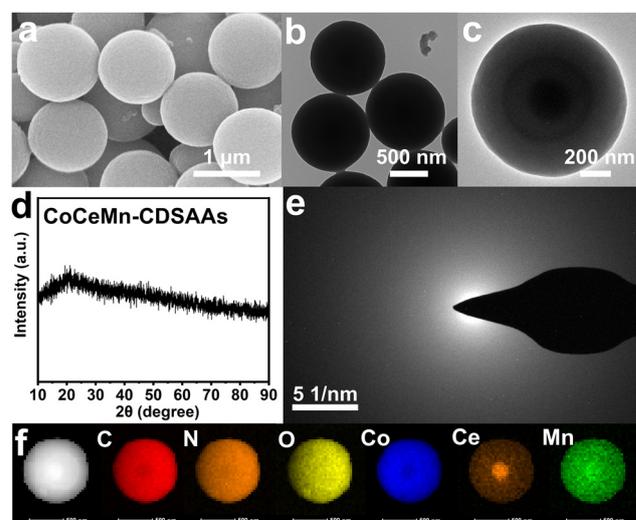
Fig. 1 (a) SEM and (b), (c) TEM images of CoCeMn-CDSAAs. (d) XRD spectrum and (e) SAED pattern of CoCeMn-CDSAAs. (f) HAADF-STEM image of CoCeMn-CDSAAs and corresponding EDX mapping of C, N, O, Co, Ce and Mn elements.

When adjusting metal ratios or synthesizing by a one-step method, the obtained nanospheres show different sizes or inhomogeneity (Fig. S2–S6, ESI†). When illustrated from a structural perspective, X-ray diffraction (XRD) and selected area electron diffraction (SAED) results both indicate that CoCeMn-CDSAA nanospheres are amorphous (Fig. 1(d) and (e)). Similarly, monometallic and bimetallic nanospheres can also be easily synthesized, and XRD patterns demonstrate that Co-CDSAAs, CoCe-CDSAAs and CoMn-CDSAAs are also amorphous (Fig. S7, ESI†). Moreover, the Fourier transform infrared (FT-IR) spectroscopy characterizations (Fig. S8, ESI†) reveal that Co-CDSAAs, CoMn-CDSAAs, CoCe-CDSAAs and CoCeMn-CDSAAs show the same IR absorption peaks, which suggest that they have the same coordination mode, and thus, they have similar morphological characteristics.[32,33] EDX elemental mapping results indicate that the Ce element enriches at the core of the sphere, while C, N, O, Co and Mn elements are uniformly distributed in the solid nanospheres (Fig. 1(f)), which is the basis for the formation of porous core–shell structures after calcination.

According to thermogravimetric (TGA) curves (Fig. S9, ESI†), CoCeMn-CDSAAs are able to form corresponding oxides after annealing at over 400 °C. Based on energy-dispersive X-ray spectroscopy (EDX) data (Table S2, ESI†), the metal ratios in the corresponding metal oxides remain consistent with the precursors. Interestingly, the high content of Ce elements can effectively strengthen their structural stability under high temperature conditions. The intensity of the diffraction peaks belonging to CeO_2 in the XRD pattern gradually decreases (Fig. S10, ESI†), which also indicates that the content of CeO_2 gradually decreases from CoCeMn-oxides-1 to CoCeMn-oxides-5. With the decrease in the content of Ce elements, the solid structure of the nanospheres starts to disappear and forms a porous core–shell structure (Fig. S11 and S12, ESI†). When the atomic ratio of Co/Ce is 8.54 in CoCeMn-CDSAAs, Mn–CeO_2@Co_3O_4 exhibits a complete porous core–shell structure after calcination (Fig. 2(a) and (b)). When the content of Ce elements continues to be reduced, the structure of CoCeMn-oxides-5 collapses (Fig. S11g and S12g, ESI†). Follow-up electrochemical active surface area (ESCA) results (Fig. S17d, ESI†) also reveal that Mn–CeO_2@Co_3O_4 possesses the most abundant electrochemical active sites among CoCeMn-oxides-x (x = 1–5), which may be due to their well-defined porous core–shell structure. Fig. 2 shows the successful formation of Mn–CeO_2@Co_3O_4 after calcination. Evidently, the diameter of Mn–CeO_2@Co_3O_4 shrinks to about 600 nm, and a porous core–shell structure is formed (Fig. 2(a)–(c)). The XRD pattern, high-resolution TEM (HRTEM) image and SAED pattern all show that there is a two-component heterogeneous structure in Mn–CeO_2@Co_3O_4 (Fig. 2(d)–(f)), which corresponds to CeO_2 (PDF#34-0394) and Co_3O_4 (PDF#43-1003), respectively. Compared with CoCe-oxides, there is a significant negative shift of Co_3O_4 (311) in Mn–CeO_2@Co_3O_4 (Fig. S13b, ESI†), which proves the successful doping of Mn elements in Co_3O_4.[34,35] In addition, the EDX elemental mapping (Fig. 2(g)) also reveals the formation of CeO_2 and Co_3O_4 heterostructures and uniform
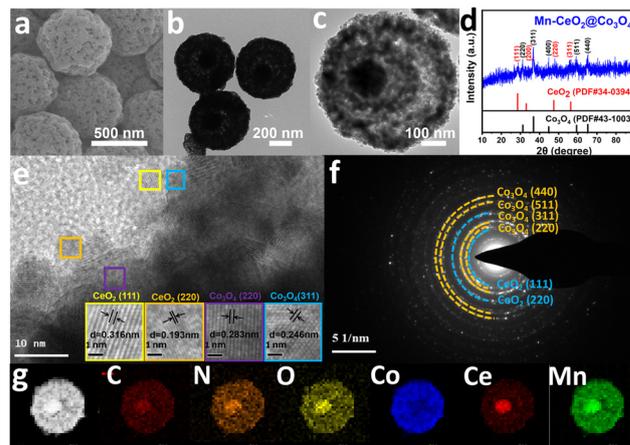

Fig. 2 (a) SEM and (b), (c) TEM images of Mn–CeO_2@Co_3O_4. (d) XRD spectrum, (e) HRTEM image and (f) SAED pattern of Mn–CeO_2@Co_3O_4. (g) HAADF-STEM image of Mn–CeO_2@Co_3O_4 and the corresponding EDX mapping of C, N, O, Co, Ce and Mn elements.

distribution of C, N, O, and Mn elements in Mn–CeO_2@Co_3O_4. When other factors are adjusted to synthesize the comparison material, the spherical morphology of CoCeMn-oxides-x (x = 6–10) are largely preserved though most of nanospheres showed unsatisfactory core–shell morphology (Fig. S4–S6, ESI†). However, the spherical morphology of Co-oxides, CoMn-oxides and CoCe-oxides was severely fragmented after calcination (Fig. S10 and S11, ESI†). All these results indicate that coexistence of Co, Ce and Mn elements is important for maintaining the spherical morphology. Moreover, a suitable metal ratio in precursors and a unique one-pot multi-step method both contribute to favorable porous core shell structures after calcination.

Modulating the electronic structure of metal atoms by heteroatom doping can effectively optimize the kinetic process of OERs.[36] Therefore, Mn–CeO_2@Co_3O_4 is selenized to further enhance its OER performance. The SEM and TEM images of the obtained MnSe–CeO_2@Co_3O_4 are shown in Fig. 3, and the porous core–shell structure of Mn–CeO_2@Co_3O_4 is preserved. As exhibited in Fig. S14 (ESI†), the surface area is about 298.67 m^2 g^{-1} and the corresponding pore size is about 4.26 nm for MnSe–CeO_2@Co_3O_4. Fig. 3(a)–(c) show that the morphology of MnSe–CeO_2@Co_3O_4 is almost unchanged after selenization, whose diameter is about 500 nm. The XRD, HRTEM and SAED results (Fig. 3(d)–(f)) all correspond to CeO_2 (PDF#34-0394) and Co_3O_4 (PDF#43-1003), revealing the presence of CeO_2 and Co_3O_4 heterostructures. In addition, there is no new diffraction peak of $CoSe_2$, which proves the successful doping of Se elements in Co_3O_4. The magnified XRD spectra show that there is almost no obvious movement for the diffraction peak belonging to Co_3O_4 (311) in MnSe–CeO_2@Co_3O_4 compared with Mn–CeO_2@Co_3O_4 (Fig. S13b, ESI†), implying that suitable elemental doping of Se elements can hardly alter the crystal structure of Mn–CeO_2@Co_3O_4.[37] EDX elemental mapping results (Fig. 3(g)) also show the presence of CeO_2 and Co_3O_4 heterostructures and the uniform distribution of C, N, O, Mn, Se elements in MnSe–CeO_2@Co_3O_4.
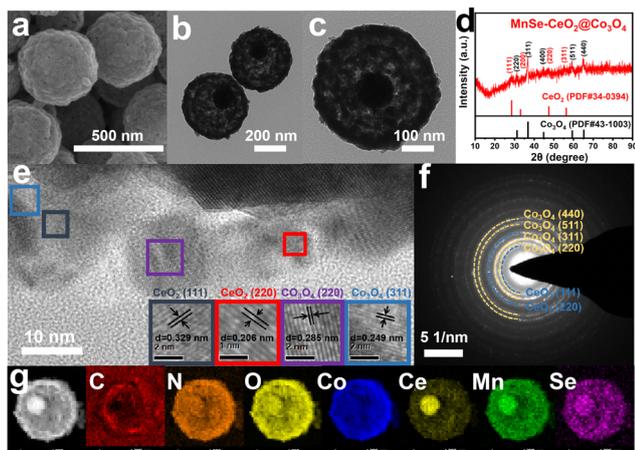
Fig. 3 (a) SEM and (b), (c) TEM images of MnSe–CeO$_2$@Co$_3$O$_4$. (d) XRD spectrum, (e) HRTEM image and (f) SAED pattern of MnSe–CeO$_2$@Co$_3$O$_4$. (g) HAADF-STEM image of MnSe–CeO$_2$@Co$_3$O$_4$ and the corresponding EDX mapping of C, N, O, Co, Ce, Mn and Se elements.

To further investigate the role of CeO$_2$ as well as the doping of Mn/Se elements in MnSe–CeO$_2$@Co$_3$O$_4$, the elements and the corresponding chemical statuses of samples were investigated by X-ray photoelectron spectroscopy (XPS). The presence of C, N, O, Co, Ce, Mn and Se elements is observed in both EDX (Fig. 4(a)) and survey spectra (Fig. 4(b)) of MnSe–CeO$_2$@Co$_3$O$_4$. The low content of Se and Mn elements in EDX spectrum can further prove their doping in MnSe–CeO$_2$@Co$_3$O$_4$. The orbital peak of Ce 3d splits into a series of Ce^{3+} and Ce^{4+} peaks, indicating that Ce^{3+} and Ce^{4+} coexist in MnSe–CeO$_2$@Co$_3$O$_4$ (Fig. 4(c)). The peaks at 885.2 and 903.9 eV are attributed to Ce^{3+}, while the peaks at 882.4, 887.8, 898.3, 901.3, 907.4, and 916.7 eV are attributed to Ce^{4+}.[38,39] The XPS spectrum of O 1s can be divided into three peaks (donated as O1, O2, and O3 in Fig. 4(d)). The O1 peak at 530.0 eV is attributed to the metal–oxygen bond in the material, the O2 peak at 531.2 eV is attributed to the oxygen vacancy and the O3 peak at 532.7 eV is attributed to the hydroxyl group adsorbed on the surface.[40]
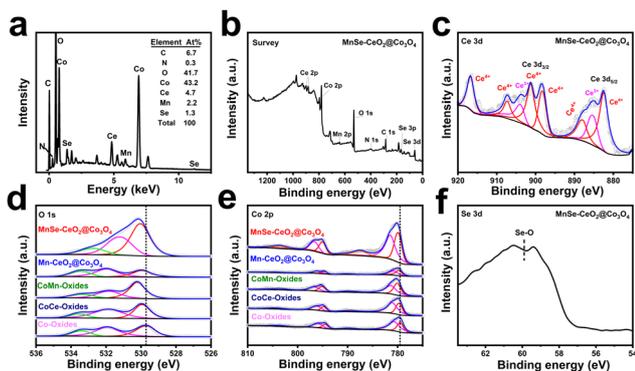
It is noteworthy that high oxygen vacancy contents can enhance the intrinsic activity of the material and optimize the kinetic properties of the OER progress.[41,42] The introduction of CeO$_2$ effectively increases the content of oxygen vacancies (Table S3, ESI†), which is useful for improving the intrinsic activity of nanomaterials. For Co 2p (Fig. 4(e)), the peaks at 796.7 and 781.5 eV correspond to Co 2p$_{1/2}$ and Co 2p$_{3/2}$ of Co^{2+}, while the peaks at 795.0 and 779.9 eV are attributed to Co 2p$_{1/2}$ and Co 2p$_{3/2}$ of Co^{3+} with the presence of two vibrational satellite peaks (787.6 and 803.6 eV).[43,44] Compared with Co-oxides, there are positive shifts in the binding energy of Co 2p$_{3/2}$ after introduction of CeO$_2$ and Mn/Se elements (Fig. 4(e)), which implies the electron transfer among different components. This phenomenon may be due to the rearrangement of electron distribution resulting from the interaction of Co with CeO$_2$ or dopants. The strong interaction in MnSe–CeO$_2$@Co$_3$O$_4$ may modulate the frontier orbital energy of the catalysts, which is useful for improving the kinetic process of OERs.[45,46] Moreover, it is worth mentioning that the doping of Mn/Se elements can significantly increase the content of Co^{3+} (Table S3, ESI†), and high activity of Co^{3+} can effectively accelerate the kinetic process of OERs.[47,48] It is obvious that a high ratio of Co^{3+}/ Co^{2+} and a high oxygen vacancy content in MnSe–CeO$_2$@Co$_3$O$_4$ are important to enhance their electrochemical performance.

At room temperature, the OER performance of the prepared catalysts is explored in an alkaline medium of 1 M KOH. It should be noticed that MnSe–CeO$_2$@Co$_3$O$_4$ is chosen as the main discussion object in the following based on that Mn–CeO$_2$@Co$_3$O$_4$, as the precursor of MnSe–CeO$_2$@Co$_3$O$_4$, is demonstrated to have the most promising performance among CoCeMn-oxides-x (x = 1–10), as observed from Fig. S17 and S19 (ESI†). As shown in Fig. 5(a), the anodic linear scanning voltammetry (LSV) polarization curves of different catalysts exhibit significant differences at a scan rate of 10 mV s^{-1}. MnSe–CeO$_2$@Co$_3$O$_4$ exhibits the optimal overpotential of 284 mV among these comparison materials, which is significantly lower than that of Co-oxides (419 mV), CoMn-oxides (390 mV), CoCe-oxides (365 mV) and Mn–CeO$_2$@Co$_3$O$_4$ (336 mV). The OER performance of trimetallic oxides is better than that of monometallic or bimetallic oxides, indicating that the synergistic effect of multiple components and the special porous core–shell structure contribute to their excellent performance. In addition, the corresponding oxides showed similar OER results after selenization (Fig. S19b, ESI†), which are attributed to the synergy of multiple components and porous core shell structure. Moreover, the OER performance of MnSe–CeO$_2$@Co$_3$O$_4$ is superior to that of commercial RuO$_2$ (362 mV) (Fig. S18, ESI†) and most recently reported Co$_3$O$_4$-based or CeO$_2$-based catalysts (Fig. 5(f) and Table S4, ESI†). The Tafel slope can further explain the OER properties from a kinetic point of view. The smaller value of Tafel slope means the faster kinetic process of OERs.[49] Among these tested catalysts, MnSe–CeO$_2$@Co$_3$O$_4$ exhibits the smallest Tafel slope of 94 mV dec^{-1}, revealing their boosting OER kinetic process (Fig. 5(b)). The ESCAs are collected to probe the actual number of active sites involved in the electrochemical reaction. The ESCAs of the

Fig. 4 (a) EDX and (b) Survey spectra of MnSe–CeO$_2$@Co$_3$O$_4$. High-resolution XPS spectra of (c) Ce 3d and (f) Se 3d in MnSe–CeO$_2$@Co$_3$O$_4$. High-resolution XPS spectra of (d) O 1s and (e) Co 2p comparison among Co-oxides, CoCe-oxides, CoMn-oxides, Mn-CeO$_2$@Co$_3$O$_4$ and MnSe–CeO$_2$@Co$_3$O$_4$.
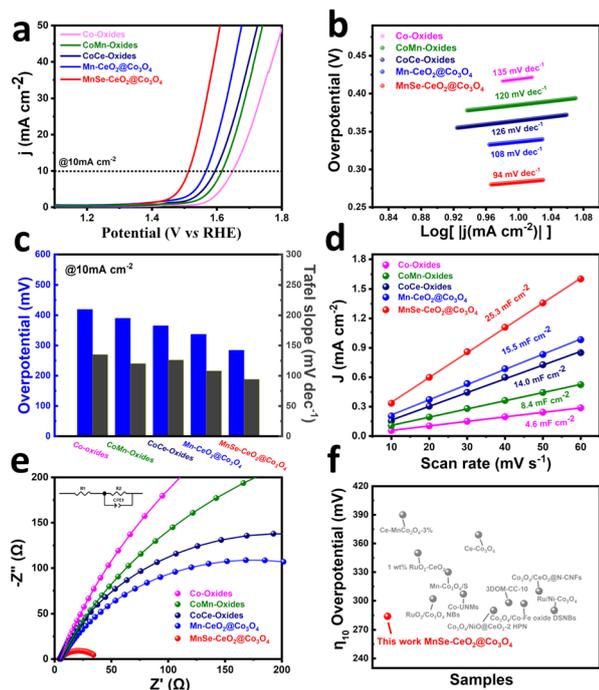
Fig. 5 (a) LSV polarization curves of Co-oxides, CoMn-oxides, CoCe-oxides, Mn−CeO$_2$@Co$_3$O$_4$ and MnSe−CeO$_2$@Co$_3$O$_4$ in 1 M KOH aqueous solution for OERs. (b) Corresponding Tafel slopes. (c) Corresponding overpotentials and Tafel slopes at 10 mA cm^{-2}. (d) Double-layer capacitance (Cdl) obtained by linear fitting of the capacitive currents. (e) EIS Nyquist plots of Co-oxides, CoMn-oxides, CoCe-oxides, Mn−CeO$_2$@Co$_3$O$_4$ and MnSe−CeO$_2$@Co$_3$O$_4$. Inset is the equivalent circuit. (f) Comparison of overpotentials at 10 mA cm^{-2} for the MnSe−CeO$_2$@Co$_3$O$_4$ catalyst with the recently reported Co-based or Ce-based OER electrocatalysts.

catalysts exhibit a positive correlation with double layer capacitance (C_{dl}) and the C_{dl} value can be obtained in the non-faradaic region with different scan rates (Fig. S20, ESI†).[50] As shown in Fig. 5(c), the C_{dl} value of MnSe−CeO$_2$@Co$_3$O$_4$ (25.3 mF cm^{-2}) is much higher than that of other catalysts, which suggests that MnSe−CeO$_2$@Co$_3$O$_4$ has more active sites under the same loading condition. Electrochemical impedance spectroscopy (EIS) value can effectively reflect the electron transfer rate and resistance value between the catalyst and the electrolyte.[51] The smaller radius of the impedance arc represents its smaller charge transfer resistance (R_{ct}), which results in the improved OER activity of the catalysts. The Nyquist curves (Fig. 5(e)) show that MnSe−CeO$_2$@Co$_3$O$_4$ has the smallest semi-circular diameter among catalysts, which means the smallest charge transfer resistance (R_{ct}) (only 34 Ω). This phenomenon indicates that there is a significant enhancement of the electrical conductivity in materials after the doping of Se elements. A series of OER tests have shown that the doping of CeO$_2$, Mn and Se elements can contribute significantly to the improvement of the OER performance. Compared with Co-oxides and CoMn-oxides, CoCe-oxides and CoCe−Mn-oxides clearly possess a lower overpotential, faster OER kinetic performance, larger electrochemically active surface area and smaller

charge transfer resistance, respectively. This is attributed to the increased oxygen vacancy content caused by the introduction of CeO$_2$. Similarly, a series of performance tests can also show that Mn and Se elements provide higher levels of Co^{3+} to the catalyst in favor of the enhanced OER performance of the catalyst.

The stability is an important parameter for evaluating their electrochemical performance, which contributes to the further practical application of the catalysts.[52,53] Cyclic voltammetry (CV) and chronopotentiometric (CP) methods are used to test the stability of MnSe−CeO$_2$@Co$_3$O$_4$. The OER polarization curve of MnSe−CeO$_2$@Co$_3$O$_4$ remains almost unchanged after 1000 CV cycles, reflecting their excellent stability (Fig. S21, ESI†). To reduce the effect of sample shedding, MnSe−CeO$_2$@Co$_3$O$_4$ dropped on an inactive carbon paper substrate for testing their OER performance. Reaching the current density of 10 mA cm^{-2}, the overpotential of MnSe−CeO$_2$@Co$_3$O$_4$ on the carbon paper is 310 mV in 1 M KOH solution (Fig. 6(a)) and the OER activity is almost unchanged after the CP test of 40 h (Fig. 6(b)). The TEM image (Fig. 6(c)) shows that the porous core–shell morphology of MnSe−CeO$_2$@Co$_3$O$_4$ is still preserved after the long-time CP test, revealing the superior structural stability of porous core–shell structures. Moreover, the main components of MnSe−CeO$_2$@Co$_3$O$_4$ are still Co$_3$O$_4$ and CeO$_2$ after stability testing (Fig. 6(d), Fig. S22 and S23, ESI†), indicating the stable composition of catalysts. The XPS spectra are employed to further
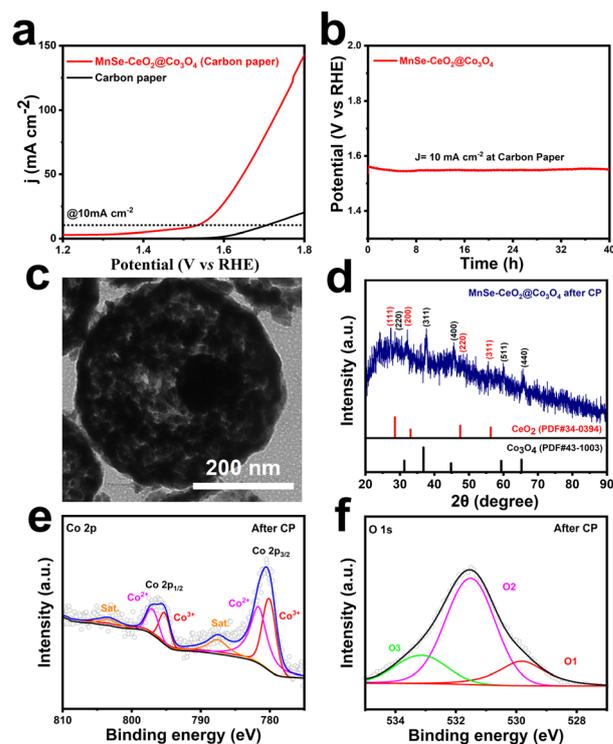

Fig. 6 (a) OER polarization curve of MnSe−CeO$_2$@Co$_3$O$_4$ loaded on the carbon paper and bare carbon paper. (b) CP curves of MnSe−CeO$_2$@Co$_3$O$_4$ loaded on the carbon paper at 10 mA cm^{-2}. (c) TEM image and (d) XRD pattern of MnSe−CeO$_2$@Co$_3$O$_4$ after the CP test. High-resolution XPS spectra of (e) Co 2p and (f) O 1s in MnSe−CeO$_2$@Co$_3$O$_4$ after the CP test.

understand the elemental valence changes of MnSe–CeO$_2$@Co$_3$O$_4$ after stability testing. It is worth noting that MnSe–CeO$_2$@Co$_3$O$_4$ still maintains a high ratio of Co^{3+}/Co^{2+} (Fig. 6(e)) and a high oxygen vacancy content (Fig. 6(f)) after the stability test, which may be the reason for their excellent stability (Table S3, ESI†).

The desirable electrochemical property of MnSe–CeO$_2$@Co$_3$O$_4$ may be attributed to the following reasons. First, BET and ESCA results both reveal that the porous core–shell structure possesses a larger specific surface area and more active sites for OERs. The large area of interfaces in contact with the electrolyte can accelerate the active intermediate transport and diffusion on the surface of catalysts, thus optimizing their catalytic capacity.[54,55] Second, high oxygen vacancy contents can strengthen the intrinsic activity of catalysts, which facilitates the reduction of the OER reaction energy barrier and optimizes their OER activity.[56] The XPS spectra illustrate that CeO$_2$ can effectively increase the content of oxygen vacancies among the above-mentioned nanomaterials (Table S3, ESI†), which is considered as one of the reasons for their favorable OER activity. Third, element doping can lead to a shift of the metal elements from a lower valence to a more active higher valence state (for instance, Co^{2+} species are oxidized to Co^{3+} species) (Table S3, ESI†). The high oxidation state of Co^{3+} can facilitate the adsorption of OER intermediates and the four-electron transfer process of OERs.[57,58] Moreover, the smallest Tafel slope of MnSe–CeO$_2$@Co$_3$O$_4$ also means a faster four-electron transfer process of OERs (Fig. 5(b)). Finally, the EIS value of MnSe–CeO$_2$@Co$_3$O$_4$ is significantly lower than that of other comparison catalysts (Fig. 5(e)). This is mainly because the introduced substances affect the coordination environment and electronic structure of the adjacent Co atoms, leading to lattice distortions and defects, which really enhance the electrical conductivity of the nanomaterials.[59] Therefore, MnSe–CeO$_2$@Co$_3$O$_4$ with the unique characteristics of morphology, structure and composition ultimately possess enhanced electrochemical properties.

3. Conclusions

In a word, a multicomponent doping strategy was proposed to fabricate MnSe–CeO$_2$@Co$_3$O$_4$ porous core–shell nanospheres with large surface area, high oxygen vacancy content, outstanding kinetic performance and excellent electrical conductivity. At a current density of 10 mA cm^{-2}, the overpotential of MnSe–CeO$_2$@Co$_3$O$_4$ is only 284 mV, which is significantly lower than that of Co-oxides (419 mV). Moreover, MnSe–CeO$_2$@Co$_3$O$_4$ exhibits a long-time stability of 40 h in 1 M KOH solution. Introduction of CeO$_2$ and doping of Mn/Se elements play an important role in elevating the oxygen vacancy level and the ratio of Co^{3+}/Co^{2+} on the surface respectively, which are beneficial to optimize the four-electron transfer process. Besides, the enhanced electrical conductivity and porous core–shell structure improve the intrinsic activity of the materials, which both ultimately enhance their OER performance. This work not

only supplies an effective catalyst with non-noble metals for OERs but also provides a meaningful reference for designing multi-component porous core–shell nanomaterials as more advanced electrocatalysts.

Conflicts of interest

There are no conflicts to declare.

Acknowledgements

References

1 Z. Seh, J. Kibsgaard, C. Dickens, I. Chorkendorff, J. Norskov and T. Jaramillo, Combining Theory and Experiment in Electrocatalysis: Insights into Materials Design, *Science*, 2017, **355**, eaad4998.

2 B. Guan, L. Yu, J. Li and X. Lou, TiO$_2$ Nanoshells with Enhanced Lithium Storage Properties, *Sci. Adv.*, 2016, **2**, e1501554.

3 T. Tian, M. Zheng, J. Lin, X. Meng and Y. Ding, Amorphous Ni–Fe Double Hydroxide Hollow Nanocubes Enriched with Oxygen Vacancies as Efficient Electrocatalytic Water Oxidation Catalysts, *Chem. Commun.*, 2019, **55**, 1044–1047.

4 Y. Jiao, Y. Zheng, M. Jaroniec and S. Qiao, Design of Electrocatalysts for Oxygen- and Hydrogen-Involving Energy Conversion Reactions, *Chem. Soc. Rev.*, 2015, **44**, 2060–2086.

5 X. Xu, F. Song, X. Hu and A. Nickel, Iron Diselenide-Derived Efficient Oxygen-Evolution Catalyst, *Nat. Commun.*, 2016, **7**, 12324.

6 Y. Hou, M. Qiu, T. Zhang, J. Ma, S. Liu, X. Zhuang, C. Yuan and X. Feng, Ternary Porous Cobalt Phosphoselenide Nanosheets: An Efficient Electrocatalyst for Electrocatalytic and Photoelectrochemical Water Splitting, *Adv. Mater.*, 2017, **29**, 1604480.

7 Y. Zhou, S. Sun, J. Song, S. Xi, B. Chen, Y. Du, A. Fisher, F. Cheng, X. Wang, H. Zhang and Z. Xu, Enlarged Co–O Covalency in Octahedral Sites Leading to Highly Efficient Spinel Oxides for Oxygen Evolution Reaction, *Adv. Mater.*, 2018, **30**, 1802912.

8 Y. Duan, S. Sun, Y. Sun, S. Xi, X. Chi, Q. Zhang, X. Ren, J. Wang, S. Ong, Y. Du, L. Gu, A. Grimaud and Z. Xu, Mastering Surface Reconstruction of Metastable Spinel Oxides for Better Water Oxidation, *Adv. Mater.*, 2019, **31**, 1807898.

9 T. Ma, S. Dai, M. Jaroniec and S. Qiao, Metal–Organic Framework Derived Hybrid Co_3O_4–Carbon Porous Nanowire Arrays as Reversible Oxygen Evolution Electrodes, *J. Am. Chem. Soc.*, 2014, **136**, 13925–13931.

10 T. Quast, S. Varhade, S. Saddeler, Y. Chen, C. Andronescu, S. Schulz and W. Schuhmann, Single Particle Nanoelectrochemistry Reveals the Catalytic Oxygen Evolution Reaction Activity of Co_3O_4 Nanocubes, *Angew. Chem., Int. Ed.*, 2021, **60**, 23444–23450.

11 S. Hung, Y. Hsu, C. Chang, C. Hsu, N. Suen, T. Chan and H. Chen, Unraveling Geometrical Site Confinement in Highly Efficient Iron-Doped Electrocatalysts toward Oxygen Evolution Reaction, *Adv. Energy Mater.*, 2018, **8**, 1701686.

12 H. Xu, J. Cao, C. Shan, B. Wang, P. Xi, W. Liu and Y. Tang, MOF-Derived Hollow CoS Decorated with CeO_x Nanoparticles for Boosting Oxygen Evolution Reaction Electrocatalysis, *Angew. Chem., Int. Ed.*, 2018, **130**, 8790–8794.

13 J. Zhou, H. Zheng, Q. Luan, X. Huang, Y. Li, Z. Xi, G. Lu, L. Xing and Y. Li, Improving the Oxygen Evolution Activity of Co_3O_4 by Introducing Ce Species Derived from Ce-substituted ZIF-67, *Sustainable Energy Fuels*, 2019, **3**, 3201–3207.

14 X. Du, Y. Ding and X. Zhang, Selectively Se-Doped Co_3O_4@CeO_2 Nanoparticle-Dotted Nanoneedle Arrays for High-Efficiency Overall Water Splitting, *Appl. Surf. Sci.*, 2021, **562**, 150227.

15 W. Li, L. Zhao, C. Wang, X. Lu and W. Chen, Interface Engineering of Heterogeneous CeO_2–CoO Nanofibers with Rich Oxygen Vacancies for Enhanced Electrocatalytic Oxygen Evolution Performance, *ACS Appl. Mater. Interfaces*, 2021, **13**, 46998–47009.

16 J. Huang, H. Sheng, R. Ross, J. Han, X. Wang, B. Song and S. Jin, Modifying Redox Properties and Local Bonding of Co_3O_4 by CeO_2 Enhances Oxygen Evolution Catalysis in Acid, *Nat. Commun.*, 2021, **12**, 3036.

17 J. Xia, H. Zhao, B. Huang, L. Xu, M. Luo, J. Wang, F. Luo, Y. Du and C. Yan, Efficient Optimization of Electron/Oxygen Pathway by Constructing Ceria/Hydroxide Interface for Highly Active Oxygen Evolution Reaction, *Adv. Funct. Mater.*, 2020, **30**, 1908367.

18 B. Qiu, C. Wang, N. Zhang, L. Cai, Y. Xiong and Y. Chai, CeO_2-Induced Interfacial Co^{2+} Octahedral Sites and Oxygen Vacancies for Water Oxidation, *ACS Catal.*, 2019, **9**, 6484–6490.

19 S. Chen, H. Huang, P. Jiang, K. Yang, J. Diao, S. Gong, S. Liu, M. Huang, H. Wang and Q. Chen, Mn-Doped RuO_2 Nanocrystals as Highly Active Electrocatalysts for Enhanced Oxygen Evolution in Acidic Media, *ACS Catal.*, 2019, **10**, 1152–1160.

20 K. Chang, D. Tran, J. Wang, N. Kim and J. Lee, A 3D Hierarchical Network Derived from 2D Fe-Doped NiSe Nanosheets/Carbon Nanotubes with Enhanced OER Performance for Overall Water Splitting, *J. Mater. Chem. A*, 2022, **10**, 3102–3111.

21 Y. Huang, J. Wang, Y. Zou, L. Jiang, X. Liu, W. Jiang, H. Liu and J. Hu, Selective Se Doping of $NiFe_2O_4$ on an Active NiOOH Scaffold for Efficient and Robust Water Oxidation, *Chin. J. Catal.*, 2021, **42**, 1395–1403.

22 S. Li, L. Wang, H. Su, A. Hong, Y. Wang, H. Yang, L. Ge, W. Song, J. Liu, T. Ma, X. Bu and P. Feng, Electron Redistributed S-Doped Nickel Iron Phosphides Derived from One-Step Phosphatization of MOFs for Significantly Boosting Electrochemical Water Splitting, *Adv. Funct. Mater.*, 2022, **32**, 202200733.

23 X. Zhang, B. Li, M. Lan, S. Yang, Q. Xie, J. Xiao, F. Xiao and S. Wang, Cation Modulation of Cobalt Sulfide Supported by Mesopore-Rich Hydrangea-Like Carbon Nanoflower for Oxygen Electrocatalysis, *ACS Appl. Mater. Interfaces*, 2021, **13**, 18683–18692.

24 C. Jiang, J. Yang, T. Zhao, L. Xiong, Z. Guo, Y. Ren, H. Qi, A. Wang and J. Tang, Co^{3+}–O–V^{4+} Cluster in $CoVO_x$ Nanorods for Efficient and Stable Electrochemical Oxygen Evolution, *Appl. Catal., B*, 2021, **282**, 119571.

25 J. Qi, H. Wang, J. Lina, C. Li, X. Si, J. Cao, Z. Zhong and J. Feng, Mn and S Dual-Doping of MOF-Derived Co_3O_4 Electrode Array Increases the Efficiency of Electrocatalytic Generation of Oxygen, *J. Colloid Interface Sci.*, 2019, **557**, 28–33.

26 Z. Cai, X. Bu, P. Wang, W. Su, R. Wei, J. Ho, J. Yang and X. Wang, Simple and Cost Effective Fabrication of 3D Porous Core–Shell Ni Nanochains@NiFe Layered Double Hydroxide Nanosheet Bifunctional Electrocatalysts for Overall Water Splitting, *J. Mater. Chem. A*, 2019, **7**, 21722–21729.

27 Y. Fu, W. Wang, J. Wang, X. Li, R. Shi, O. Peng, B. Chandrashekar, K. Liu, A. Amini and C. Cheng, MOFs-Derived ZnCo–Fe Core–Shell Nanocages with Remarkable Oxygen Evolution Reaction Performance, *J. Mater. Chem. A*, 2019, **7**, 17299–17305.

28 X. Yang, Y. Zhang, Y. Wang, C. Xin, P. Zhang, D. Liu, B. Mamba, K. Kefeni, A. Kuvarega and J. Gui, Hollow β-Bi_2O_3@CeO_2 Heterostructure Microsphere with Controllable Crystal Phase for Efficient Photocatalysis, *Chem. Eng. J.*, 2020, **387**, 124100.

29 D. An, J. Wang, J. Zhang, X. Zhai, Z. Kang, W. Fan, J. Yan, Y. Liu, L. Lu, C. Jia, M. Wuttig, O. Cojocaru-Miredin, S. Chen, W. Wang, G. Snyder and Y. Yu, Retarding Ostwald Ripening through Gibbs Adsorption and Interfacial Complexions Leads to High-Performance SnTe Thermoelectrics, *Energy Environ. Sci.*, 2021, **14**, 5469–5479.

30 J. Liu, Z. Wang, Y. Chai, M. Kurmoo, Q. Zhao, X. Wang, C. Tung and D. Sun, Core Modulation of 70-Nuclei Core–Shell Silver Nanoclusters, *Angew. Chem., Int. Ed.*, 2019, **58**, 6276–6279.

31 L. Zhang, L. Zhang, G. Xu, C. Zhang, X. Li, Z. Sun and D. Jia, Low-Temperature CO Oxidation over CeO_2 and CeO_2@ Co_3O_4 Core–Shell Microspheres, *New J. Chem.*, 2017, **41**, 13418–13424.

32 Y. Zhao, J. Zhang, J. Song, J. Li, J. Liu, T. Wu, P. Zhang and B. Han, Ru Nanoparticles Immobilized on Metal–Organic Framework Nanorods by Supercritical CO_2–Methanol Solution: Highly Efficient Catalyst, *Green Chem.*, 2011, **13**, 2078–2082.

33 X. Huang, C. Zhou, H. Liu, L. Zeng, X. Zhang, X. Han, F. Zhu, Y. Lu, X. Cao and H. Gu, In Situ Simultaneous

Cavitation-Doping Approach for Constructing Bimetallic Metal–Organic Framework Hollow Nanospheres with Enhanced Electrocatalytic Hydrogen Production, *Inorg. Chem.*, 2022, **61**, 5977–5981.

34 G. Li, M. Chen, Y. Ouyang, D. Yao, L. Lu, L. Wang, X. Xia, W. Lei, S. Chen, D. Mandler and Q. Hao, Manganese Doped Co_3O_4 Mesoporous Nanoneedle Array for Long Cycle-stable Supercapacitors, *Appl. Surf. Sci.*, 2019, **469**, 941–950.

35 C. Huang, Y. Zhang, X. Li, H. Cao, Y. Guo and C. Zhang, Mn-Incorporated Co_3O_4 Bifunctional Electrocatalysts for Zinc–Air Battery Application: An Experimental and DFT Study, *Appl. Catal., B*, 2022, **319**, 121909.

36 Y. Huang, L. Jiang, B. Shi, K. Ryan and J. Wang, Highly Efficient Oxygen Evolution Reaction Enabled by Phosphorus Doping of the Fe Electronic Structure in Iron–Nickel Selenide Nanosheets, *Adv. Sci.*, 2021, **8**, e2101775.

37 R. Li, Y. Guo, H. Chen, K. Wang, R. Tan, B. Long, Y. Tong, P. Tsiakaras, S. Song and Y. Wang, Anion–Cation Double Doped Co_3O_4 Microtube Architecture to Promote High-Valence Co Species Formation for Enhanced Oxygen Evolution Reaction, *ACS Sustainable Chem. Eng.*, 2019, **7**, 11901–11910.

38 L. Lv, D. Zha, Y. Ruan, Z. Li, X. Ao, J. Zheng, J. Jiang, H. Chen, W. Chiang, J. Chen and C. Wang, A Universal Method to Engineer Metal Oxide–Metal–Carbon Interface for Highly Efficient Oxygen Reduction, *ACS Nano*, 2018, **12**, 3042–3051.

39 S. Putla., M. Amin., B. Reddy., A. Nafady., K. Al Farhan. and S. Bhargava, MnO_X Nanoparticle-Dispersed CeO_2 Nanocubes: A Remarkable Heteronanostructured System with Unusual Structural Characteristics and Superior Catalytic Performance, *ACS Appl. Mater. Interfaces*, 2015, **7**, 16525–16535.

40 Q. Zhou, Y. Chen, G. Zhao, Y. Lin, Z. Yu, X. Xu, X. Wang, H. Liu, W. Sun and S. Dou, Active-Site-Enriched Iron-Doped Nickel/Cobalt Hydroxide Nanosheets for Enhanced Oxygen Evolution Reaction, *ACS Catal.*, 2018, **8**, 5382–5390.

41 S. Guo, J. Wang, Y. Sun, L. Peng and C. Li, Interface Engineering of Co_3O_4/CeO_2 Heterostructure *in situ* Embedded in Co/N-Doped Carbon Nanofibers Integrating Oxygen Vacancies as Effective Oxygen Cathode Catalyst for $Li–O_2$ Battery, *Chem. Eng. J.*, 2022, **452**, 39317.

42 D. Ghosh, M. Manikanta Kumar, C. Raj and D. Pradhan, Bifunctional Catalytic Activity of Solvothermally Synthesized CeO_2 Nanosphere/NiO Nanoflake Nanocomposites, *ACS Appl. Energy Mater.*, 2022, **5**, 5666–5679.

43 A. Saad, D. Liu, Y. Wu, Z. Song, Y. Li, T. Najam, K. Zong, P. Tsiakaras and X. Cai, Ag Nanoparticles Modified Crumpled Borophene Supported Co_3O_4 Catalyst Showing Superior Oxygen Evolution Reaction (OER) performance, *Appl. Catal., B*, 2021, **298**, 120529.

44 X. Yang, J. Chen, Y. Chen, P. Feng, H. Lai, J. Li and X. Luo, Novel Co_3O_4 Nanoparticles/Nitrogen-Doped Carbon Composites with Extraordinary Catalytic Activity for Oxygen Evolution Reaction (OER), *Nano-Micro Lett.*, 2018, **10**, 1–11.

45 M. Gong, Y. Li, H. Wang, Y. Liang, J. Wu, J. Zhou, J. Wang, T. Regier, F. Wei and H. Dai, An Advanced Ni–Fe Layered Double Hydroxide Electrocatalyst for Water Oxidation, *J. Am. Chem. Soc.*, 2013, **135**, 8452–8455.

46 Y. Guo, J. Tang, J. Henzie, B. Jiang, W. Xia, T. Chen, Y. Bando, Y. Kang, M. Hossain, Y. Sugahara and Y. Yamauchi, Mesoporous Iron-Doped $MoS_2/CoMo_2S_4$ Heterostructures through Organic Metal Cooperative Interactions on Spherical Micelles for Electrochemical Water Splitting, *ACS Nano*, 2020, **14**, 4141–4152.

47 Y. Bi, Z. Cai, D. Zhou, Y. Tian, Q. Zhang, Q. Zhang, Y. Kuang, Y. Li, X. Sun and X. Duan, Understanding the Incorporating Effect of Co^{2+}/Co^{3+} in NiFe-layered Double Hydroxide for Electrocatalytic Oxygen Evolution Reaction, *J. Catal.*, 2018, **358**, 100–107.

48 Z. Hao, P. Wei, Y. Yang, J. Sun, Y. Song, D. Guo and L. Liu, Self-Assembled $CuCo_2S_4$ Nanosheets with Rich Surface Co^{3+} as Efficient Electrocatalysts for Oxygen Evolution Reaction, *Appl. Surf. Sci.*, 2021, **536**, 147826.

49 L. Xu, Q. Jiang, Z. Xiao, X. Li, J. Huo, S. Wang and L. Dai, Plasma-Engraved Co_3O_4 Nanosheets with Oxygen Vacancies and High Surface Area for The Oxygen Evolution Reaction, *Angew. Chem., Int. Ed.*, 2016, **128**, 5363–5367.

50 Y. Zhao, C. Mavrokefalos, P. Zhang, R. Erni, J. Li, C. Triana and G. Patzke, Self-Templating Strategies for Transition Metal Sulfide Nanoboxes as Robust Bifunctional Electrocatalysts, *Chem. Mater.*, 2020, **32**, 1371–1383.

51 Y. Lu, D. Fan, Z. Chen, W. Xiao, C. Cao and X. Yang, Anchoring Co_3O_4 Nanoparticles on MXene for Efficient Electrocatalytic Oxygen Evolution, *Sci. Bull.*, 2020, **65**, 460–466.

52 J. Kang, X. Qiu, Q. Hu, J. Zhong, X. Gao, R. Huang, C. Wan, L. Liu, X. Duan and L. Guo, Valence Oscillation and Dynamic Active Sites in Monolayer NiCo Hydroxides for Water Oxidation, *Nat. Catal.*, 2021, **4**, 1050–1058.

53 F. Tang, S. Guo, Y. Sun, X. Lin, J. Qiu and A. Cao, Facile Synthesis of Fe-Doped CoO Nanotubes as High-Efficient Electrocatalysts for Oxygen Evolution Reaction, *Small Struct.*, 2022, **3**, 2100211.

54 Q. Qin, J. Hao and W. Zheng, Ni/Ni_3C Core/Shell Hierarchical Nanospheres with Enhanced Electrocatalytic Activity for Water Oxidation, *ACS Appl. Mater. Interfaces*, 2018, **10**, 17827–17834.

55 Q. Hu, Z. Wang, X. Huang, Y. Qin, H. Yang, X. Ren, Q. Zhang, J. Liu, M. Shao and C. He, Integrating Well-Controlled Core–Shell Structures into "Superaerophobic" Electrodes for Water Oxidation at Large Current Densities, *Appl. Catal., B*, 2021, **286**, 119920.

56 B. Zhang, J. Shan, X. Wang, Y. Hu and Y. Li, Ru/Rh Cation Doping and Oxygen-Vacancy Engineering of FeOOH Nanoarrays@$Ti_3C_2T_x$ MXene Heterojunction for Highly Efficient and Stable Electrocatalytic Oxygen Evolution, *Small*, 2022, **18**, e2200173.

57 D. Shao, P. Li, R. Zhang, C. Zhao, D. Wang and C. Zhao, One-Step Preparation of Fe-Doped $Ni_3S_2/rGO@NF$ Electrode and Its Superior OER Performances, *Int. J. Hydrogen Energy*, 2019, **44**, 2664–2674.

58 S. Li, S. Peng, L. Huang, X. Cui, A. Al-Enizi and G. Zheng, Carbon-Coated Co^{3+}-Rich Cobalt Selenide Derived from ZIF-67 for Efficient Electrochemical Water Oxidation, *ACS Appl. Mater. Interfaces*, 2016, **8**, 20534–20539.

59 S. Balaghi, C. Triana and G. Patzke, Molybdenum-Doped Manganese Oxide as a Highly Efficient and Economical Water Oxidation Catalyst, *ACS Catal.*, 2020, **10**, 2074–2087.